Multistep structural transformation of a magnetic metal-organic framework: possible transformation mechanism, form evolution and magnetic properties

Dong-Li, Meng,[a] Xue Wang,[c] Chong-Bin Tian,*[b] Wei Wei[b] and Shao-Wu Du*[a]

[a] *Provincial Key Laboratory of Functional Marine Sensing Materials, Minjiang University, Fujian, Fuzhou 350108, P. R. China. E-mail: swdu@fjirsm.ac.cn*

[b] *State Key Laboratory of Structural Chemistry, Fujian Institute of Research on the Structure of Matter, Chinese Academy of Sciences, Fujian, Fuzhou 350002, P. R. China. E-mail: tianchongbin@fjirsm.ac.cn*

[c] *Yantai Branched Center of Shandong Technology Transfer Center, Chinese Academy of Sciences, Shandong, Yantai 264000, P. R. China.*

Contents

1 Experimental Section.

1.1 Crystal structure analysis

2 Results and Discussion

2.1 Thermogravimetric analysis

2.2 Magnetic Susceptibility Analysis of **1** and **5**

3 Tables, Scheme and Figures

Table S1. Crystallographic data for **1**, **4** and **5**.

Table S2. Selected Bond Lengths (Å) and Angles (º) for **1**.

Table S3. Selected Bond Lengths (Å) and Angles (º) for **4**.

Table S4. Selected Bond Lengths (Å) and Angles (º) for **5**.

Table S5. Structural and Magnetic Parameters for $\{Mn_3(O_2CR)_6\}$ based Compounds.

Scheme S1. The three bridging modes of $\{Mn_3(O_2CR)_6\}$ unit.

Scheme S2. The magnetic exchange model of Mn^{II}_3 in **1**.

Figure S1. The TG curves of **1** and **5**.

Figure S2. View of the coordination environment of Mn^{2+} ions and Li^+ ions in **1** (a) and the chain structure along the *a*-axis (b). View of the coordination environment of Mn^{2+} ions in **4** (c) and the chain structure along the *a*-axis (d). View of the coordination environment of Mn^{2+} ions in **5** (e) and the chain structure along the *c*-axis (f).

Figure S3. The 6-connected α-Po network of **1** (a), **4** (b) and the $CdSO_4$ topological network of **5** (c).

Figure S4. The SEM images of **1** (a), **1-1h** (b), **1-12h** (c), **1-2d** (d), **1-5d** (e), **1-8d** (f), **1-11d** (g) and **5** (h). Scale bar: 100 μm.

Figure S5. The SEM images of large single crystal **1-1h** cut by knife manually (a), and (b), (c), (d) images are the zoomed-in images of the red, green and blue circles in the corresponding region of (a).

Figure S6. The SEM images of large single crystal **1-12h** (a) and **1-24h** (e) cut by knife manually, and (b), (c), (d) images are the zoomed-in images of the red circle, green circle and blue circle in the corresponding region of (a), while (f), (g) images are the zoomed-in images of red circle and green circle in the corresponding region of (e). (h) PXRD patters of **1** and its corresponding sample with different immersing

time.

Figure S7. Plots of $1/x_m$ vs. T in the 2−300 K temperature range for **1** (a) and for **5** (b). The red solid line is the best fit to the Curie-Weiss law above 10 K for **1** and above 40 K for **5**.

Figure S8. X-band EPR spectra of **1**, **1-1h**, **1-12h**, **1-2d**, **1-5d**, **1-8d**, **1-11d** and **5** measured at room temperature.

Figure S9. EPR spectra of methanol solvent after immersion sample **1** for 12 h.

4 Supplementary References

1 Experimental section

1.1 Crystal structure analysis

Suitable single crystals of the compounds were carefully selected and glued to thin glass fibers with epoxy resin. Intensity data were collected at room temperature on a Rigaku 70 CCD for **1** and 724 CCD for **4** and **5**, respectively, with a graphite monochromator utilizing Mo Kα radiation (λ = 0.71073 Å). *CrystalClear* software was used for data reduction and empirical absorption correction. The structures were solved by direct methods using SHELXS-97[1] and refined by full-matrix least-squares on F^2 using SHELXL-2016 program.[2] The non-hydrogen atoms were refined anisotropically for **1**, **4** and **5**, except for C26 and C30 of **1** and C33, C39, C40 of **4**. Generally, C-bound H atoms were placed geometrically and refined as riding, whereas H atoms on coordinated water molecules in **5** were located from the D−F maps, assigned isotropic thermal parameters, and allowed to ride on their respective parent atoms before the final cycle of least-squares refinement. Crystallographic data and other pertinent information for **1**, **4** and **5**, were summarized in Table S1. In **1**, one of the coordinated DMF molecule was disordered and was refined as two DMF molecules with the occupancies of 0.56 and 0.43, i.e., O10, C28, N2, C29, C30 and O10', C28', N2', C29', C30'. Moreover, some constraints (SIMU and DFIX) were applied to the coordinated DMF molecules to obtain the chemical-reasonable models and reasonable atomic displacement parameters. For **4**, some constraints (SADI, SIMU and DFIX) were used to the $TBIP^{2-}$ anions to obtain the chemical-reasonable models and reasonable atomic displacement parameters. Since the position of the disorder guest solvent molecules in **5** could not be resolved from D−F maps, SQUEEZE/PLATON was used to compensate the data for their contribution to the diffraction patterns.[3] The final chemical formula of **5** was obtained by the TGA and elemental analysis data. The CCDC numbers: 1576730(**1**), 1576731(**4**) and 1576732(**5**).

2 Results and Discussion

2.1 Thermogravimetric Analysis

To investigate the thermal stability of **1** and **5**, thermal analysis has been carried out

on crystalline sample in a nitrogen atmosphere at a heating rate of 10 °C min^{-1} (**Figure S1**). The TGA curve of **1** indicates that there is a weight loss of 22.14% from 40 to 348 °C, which can be attributed to the loss of four coordinated DMF molecules (calcd. 21.63%). For **5**, the loss (31.36%) from 40 to 290 °C corresponds to the loss of seven H_2O molecules (calcd. 31.43%). Given there are three coordinated H_2O molecules in the asymmetric unit of **5**, the other four H_2O molecules should be located in the channel of **5** as guest solvents. This result is in accordance with the result of elemental analysis. Anal. Calcd. (%) for **5** $C_{12}H_{26}O_{11}Mn$ (401.27): C 35.92, H 6.53. Found: C 36.38, H 6.28.

2.2 Magnetic Susceptibility Analysis of 1 and 5

The analysis of the magnetic data for **1** was performed based on the Hamiltonian $H = -2J_1(S_1S_2+S_2S_3) - 2J_2S_1S_3$, and the expression of the magnetic susceptibility (x_{tri}) can be written as:

$$x_{tri} = (Ng^2\beta^2/12KT)*(A/B)$$

With A = 680exp[(55J_1 + 30J_2)/KT] + 455exp[(40J_1 + 30J_2)/KT] + 286exp[(27J_1 + 30J_2)/KT] + 165exp[(16J_1 + 30J_2)/KT] + 84exp[(7J_1 + 30J_2)/KT] + 35exp(30J_2/KT) + 455[(50J_1 + 20J_2)/KT] + 286exp[(37J_1 + 20J_2)/KT] + 165exp[(26J_1 + 20J_2)/KT] + 84exp[(17J_1 + 20J_2)/KT] + 35exp[(10J_1 + 20J_2)/KT] + 10exp[(5J_1 + 20J_2)/KT] + 286exp[(45J_1 + 12J_2)/KT] + 165exp[(34J_1 + 12J_2)/KT] + 84exp[(35J_1 + 12J_2)/KT] + 35exp[(18J_1 + 12J_2)/KT] + 10exp[(13J_1 + 12J_2)/KT] + exp[(10J_1 + 12J_2)/KT] 165exp[(40J_1 + 6J_2)/KT] + 84exp[(31J_1 + 6J_2)/KT] + 35exp[(24J_1 + 6J_2)/KT] + 10exp[(19J_1 + 6J_2)/KT] + exp[(16J_1 + 6J_2)/KT] + 84exp[(35J_1 + 2J_2)/KT] + 35exp[(28J_1 + 2J_2)/KT] + 10exp[(23J_1 + 2J_2)/KT] + 35exp(30J_1/KT), and B = 8exp[(55J_1 + 30J_2)/KT] + 7exp[(40J_1 + 30J_2)/KT] + 6exp[(27J_1 + 30J_2)/KT] + 5exp[(16J_1 + 30J_2)/KT] + 4exp[(7J_1 + 30J_2)/KT] + 3exp(30J_2/KT) + 7exp[(50J_1 + 20J_2)/KT] + 6exp[(37J_1 + 20J_2)/KT] + 5exp[(26J_1 + 20J_2)/KT] + 4exp[(17J_1 + 20J_2)/KT] + 3exp[(10J_1 + 20J_2)/KT] + 2exp[(5J_1 + 20J_2)/KT] + 6exp[(45J_1 + 12J_2)/KT] + 5exp[(34J_1 + 12J_2)/KT] + 4exp[(25J_1 + 12J_2)/KT] + 3exp[(18J_1 + 12J_2)/KT] + 2exp[(13J_1 + 12J_2)/KT] + exp[(10J_1 + 12J_2)/KT] + 5exp[(40J_1 + 6J_2)/KT] + 4exp[(31J_1 + 6J_2)/KT] + 3exp[(24J_1 + 6J_2)/KT] + 2exp[(19J_1 + 6J_2)/KT] + exp[(16J_1 +

$6J_2)/KT] + 4\exp[(35J_1 + 2J_2)/KT] + 3\exp[(28J_1 + 2J_2)/KT] + 2\exp[(23J_1 + 2J_2)/KT] + 3\exp[30J_1/KT]$.

If consider the molecular field approximation, the magnetic susceptibility can be written as $x_m = x_{tri}/[1-(2zJ'/Ng^2\beta^2)]$, where z is the numbers of nearest neighbors of the trimer unit.

For **5**, the corresponding magnetic susceptibility is $x_m = [Ng\beta S(S + 1)/3KT][(1 + u)/(1 - u)]$, in which $u = \coth(JS(S + 1)/KT) - (KT/(JS(S + 1)))$, and the N, g, β and K have their usually meanings.

3 Tables, Schemes and Figures.

Table S1. Crystallographic data for **1**, **4** and **5**.

	1	**4**	**5**
empirical formula	$C_{60}H_{76}Li_2Mn_3N_4O$	$C_{40}H_{52}Mn_3O_{16}$	$C_{12}H_{26}MnO_{11}$
fw	1351.94	953.63	401.27
crystal system	monoclinic	monoclinic	tetragonal
space group	*P*21/*c*	*P*2/*c*	$P\bar{4}2_1c$
a/Å	9.533 (2)	21.25(2)	22.3208(4)
b/Å	20.341 (4)	13.033(13)	22.3208(4)
c/Å	17.725 (4)	17.219(17)	8.1027(2)
α/°	90.00	90.00	90.00
β/°	105.355 (3)	99.69(2)	90.00
γ/°	90.00	90.00	90.00
V/Å^3	3314.5 (12)	4701(8)	4036.91(18)
Z	2	4	8
D_{calc}/g cm^{-3}	1.335	1.347	1.32
μ/mm^{-1}	0.635	0.857	0.700
F(000)	1410	1980	1688
Parameters	461	559	182
R_1[a],wR_2[b] [I>2σ(I)]	0.0715/0.1932	0.1685/0.4262	0.0376/0.1092
R_1[a],wR_2[b] [all data]	0.0824/0.2046	0.1979/0.4439	0.0413/0.1113
Good-of-fiton F^2	1.069	1.012	1.022
Flack parameter			0.021(14)

[a] $R_1 = \sum\|F_o| - |F_c\|/\sum|F_o|$, [b] $wR_2 = [\sum w(F_o^2-F_c^2)^2/\sum w(F_o^2)^2]^{0.5}$.

Table S2. Selected Bond Lengths (Å) and Angles (°) for **1**.

Li1−O4	1.908 (7)	Li1−O5A	1.941 (7)
Li1−O9	1.926 (7)	Li1−O10	1.945 (11)

Mn1−O1	2.282 (2)	Mn1−O2	2.341 (2)
Mn1−O3	2.279 (2)	Mn1−O4	2.201 (2)
Mn1−O6A	2.265 (2)	Mn1−O7B	2.146 (2)
Mn2−O1	2.205 (2)	Mn2−O6A	2.193 (2)
Mn2−O8B	2.058 (2)	Mn1−Mn2	3.293(2)
O4−Li1−O9	114.4 (3)	O4−Li1−O10	106.6 (5)
O4−Li1−O5A	93.8 (3)	O9−Li1−O10	118.2 (5)
O9−Li1−O5A	108.2 (4)	O5A−Li1−O10	113.1 (5)
O4−Mn1−O7B	99.68 (9)	O2−Mn1−O4	99.05 (9)
O6A−Mn1−O7B	88.91 (9)	O2−Mn1−O6A	89.22 (9)
O4−Mn1−O6A	124.12 (9)	O2−Mn1−O3	91.57 (9)
O3−Mn1−O7B	89.33 (9)	O1−Mn1−O2	56.82 (8)
O3−Mn1−O4	58.52 (8)	O1−Mn1−O6A	77.12 (8)
O1−Mn1−O7B	101.97 (8)	O1−Mn1−O3	100.96 (8)
O6D−Mn2−O8C	90.12 (9)	O1E−Mn2−O6A	99.76 (8)
O1E−Mn2−O8C	84.80 (8)	O1−Mn2−O8C	95.20 (8)
O1E−Mn2−O8B	95.20 (8)	Li1−O4−Mn1	101.6 (2)
Mn1−O1−Mn2	94.43 (8)	Mn1F−O6−Mn2G	95.23 (8)

Symmetry codes: (A) $x, -y + 3/2, z + 1/2$; (B) $x + 1, y, z$; (C) $-x + 1, -y + 1, -z$; (D) $-x + 2, y - 1/2, -z - 1/2$; (E) $-x + 2, -y + 1, -z$; (F) $x, -y + 3/2, z - 1/2$; (G) $-x + 2, y + 1/2, -z - 1/2$.

Table S3. Selected Bond Lengths (Å) and Angles (º) for **4**.

Mn1−O2	2.122 (14)	Mn1−O4A	2.089 (12)
Mn1−O10	2.121 (12)	Mn1−O13	2.175 (13)
Mn2−O3A	2.173 (13)	Mn2−O7B	2.150 (13)
Mn2−O9	2.125 (15)	Mn2−O11	2.133 (12)
Mn2−O14	2.223 (14)	Mn2−O15	2.228 (13)
Mn3−O6	2.150 (15)	Mn3−O8B	2.090 (12)
Mn3−O12	2.130 (13)	Mn3−O16	2.157 (13)
O2−Mn1−O10	103.7 (5)	O2−Mn1−O13	111.9 (5)
O2−Mn1−O4A	135.2 (5)	O10−Mn1−O4A	104.6 (5)
O10−Mn1−O13	88.7 (5)	O13−Mn1−O4A	102.8 (6)
O9−Mn2−O3A	88.1 (6)	O9−Mn2−O7B	87.9 (5)
O9−Mn2−O15	87.7 (6)	O9−Mn2−O14	91.3 (6)
O11−Mn2−O7B	87.5 (5)	O11−Mn2−O14	88.5 (5)
O11−Mn2−O15	96.9 (6)	O11−Mn2−O3A	92.8 (5)
O14−Mn2−O15	85.7 (5)	O3A−Mn2−O15	85.0 (5)

O7B−Mn2−O3A	98.3 (6)	O7B−Mn2−O14	90.9 (5)
O6−Mn3−O8B	131.1 (6)	O6−Mn3−O12	97.1 (6)
O6−Mn3−O16	105.6 (6)	O12−Mn3−O8B	121.5 (6)
O12−Mn3−O16	90.8 (5)	O16−Mn3−O8B	102.8 (5)

Symmetry codes: (A) $x, -y+1, z-1/2$; (B) $x, -y, z-1/2$.

Table S4. Selected Bond Lengths (Å) and Angles (º) for **5**.

Mn1−O1	2.153 (3)	Mn1−O4A	2.154 (3)
Mn1−O1W	2.241 (3)	Mn1−O2W	2.168 (3)
Mn1−O3W	2.166 (3)	Mn1−O1WB	2.238 (3)
O1−Mn1−O4A	179.28 (12)	O1−Mn1−O3W	89.41 (13)
O2W−Mn1−O4A	89.12 (13)	O2W−Mn1−O3W	179.50 (13)
O1−Mn1−O2W	90.23 (13)	O1WB−Mn1−O4A	89.76 (10)
O3W−Mn1−O4A	91.24 (13)	O1−Mn1−O1WB	89.94 (9)
Mn1−O1W−Mn1C	129.52 (11)		

Symmetry codes: (A) $-x+1/2, y-1/2, -z+3/2$; (B) $-y+1/2, -x+1/2, z+1/2$; (C) $-y+1/2, -x+1/2, z-1/2$; (D) $-x+1/2, y+1/2, -z+3/2$;

Table S5. Structural and Magnetic Parameters for $\{Mn_3(O_2CR)_6\}$ based Compounds.

Bridging mode	No	type	Mn-Mn distance (Å)	g	J (cm^{-1})	ref
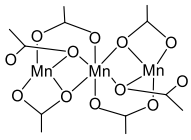	1	bis-monatomic/ syn-syn	3.293	1.96	−0.618	This work
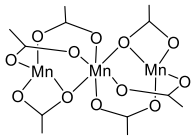	I	monatomic/ bis-(syn-syn)	3.603	2.05	−3.2	4
	II		3.611	2.02	−2.69	5
	III		3.614	1.99	−2.20	6
	IV		3.630	2.02	−2.90	7
	V		3.603	1.99	−2.74	8
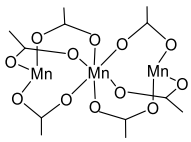	VI	tris-(syn-syn)	4.303	2.002	−7.744	9

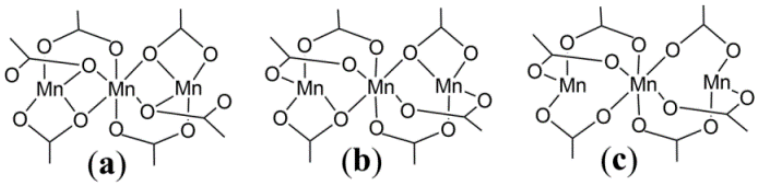

Scheme S1. The three bridging modes of $\{Mn_3(O_2CR)_6\}$ unit.

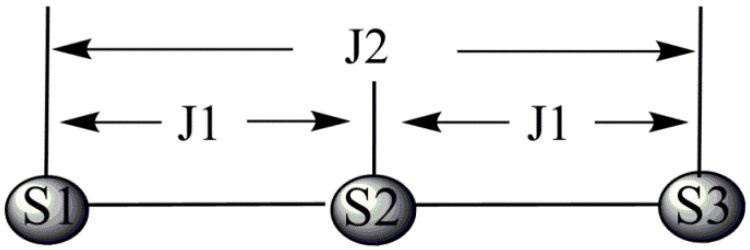

Scheme S2. The magnetic exchange model of Mn^{II}_3 in **1**.

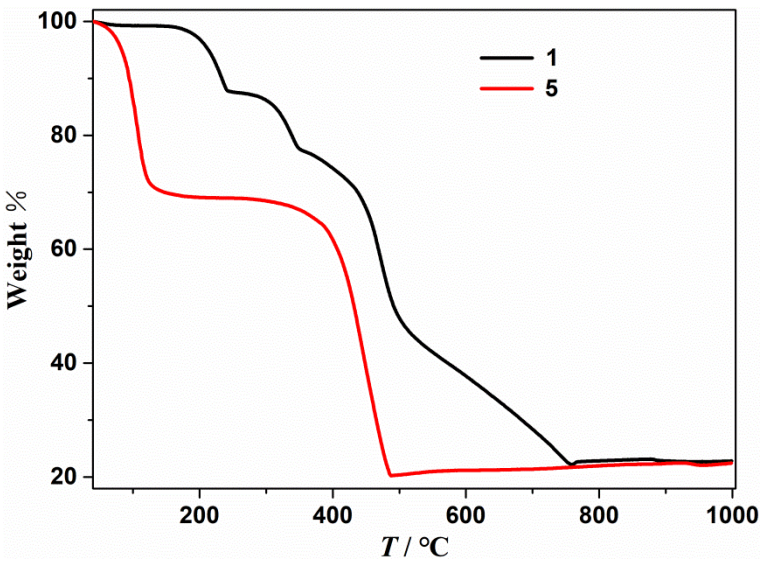

Figure S1. The TG curves of **1** and **5**.

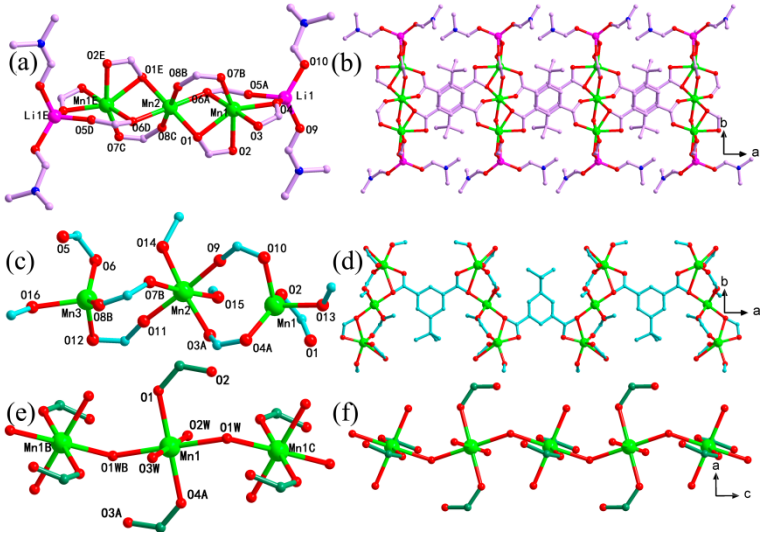

Figure S2. View of the coordination environment of Mn^{2+} ions and Li^{+} ions in **1** (a) and the chain structure along the *a*-axis (b). View of the coordination environment of Mn^{2+} ions in **4** (c) and the chain structure along the *a*-axis (d). View of the coordination environment of Mn^{2+} ions in **5** (e) and the chain structure along the *c*-axis (f).

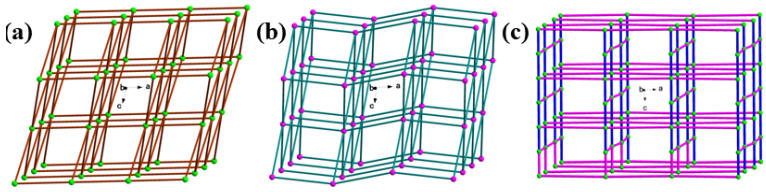

Figure S3. The 6-connected α-Po network of **1** (a), **4** (b) and the $CdSO_4$ topological network of **5** (c).

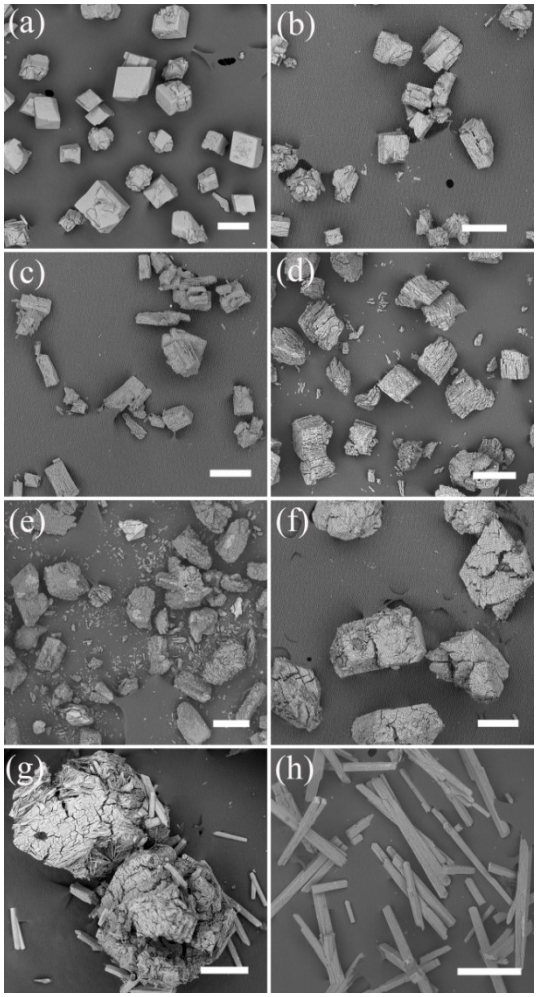

Figure S4. The SEM images of **1** (a), **1-1h** (b), **1-12h** (c), **1-2d** (d), **1-5d** (e), **1-8d** (f), **1-11d** (g) and **5** (h). Scale bar: 100 μm.

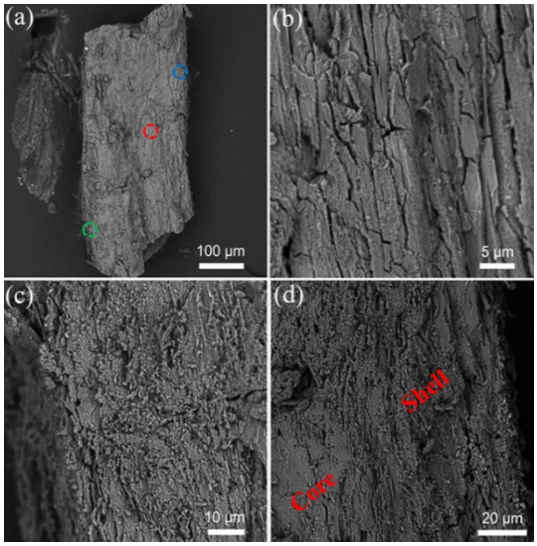

Figure S5. The SEM images of large single crystal **1-1h** cut by knife manually (a), and (b), (c), (d) images are the zoomed-in images of the red, green and blue circles in the corresponding region of (a).

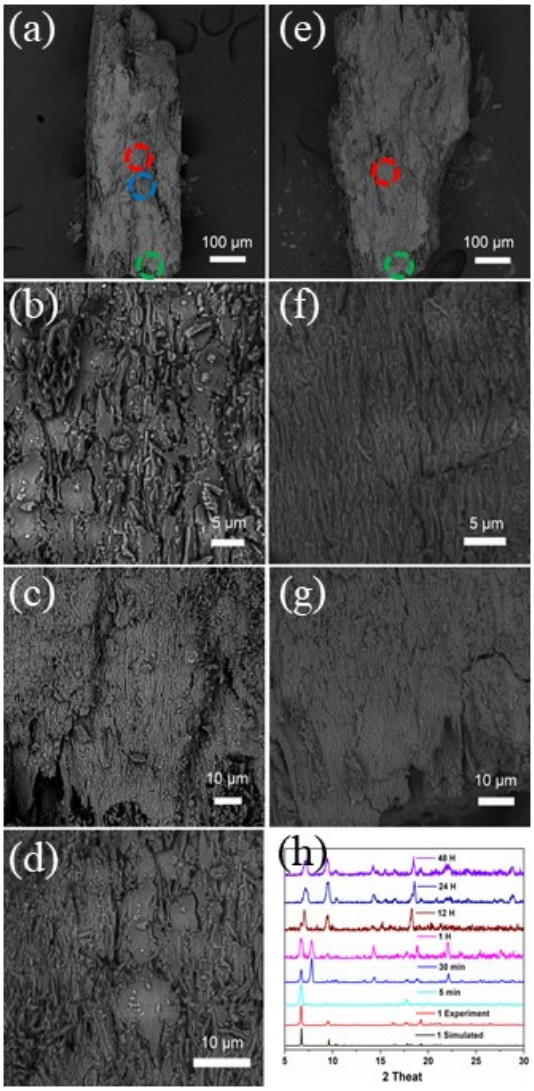

Figure S6. The SEM images of large single crystal **1-12h** (a) and **1-24h** (e) cut by knife manually, and (b), (c), (d) images are the zoomed-in images of the red circle, green circle and blue circle in the corresponding region of (a), while (f), (g) images are the zoomed-in images of red circle and green circle in the corresponding region of (e). (h) PXRD patters of **1** and its corresponding sample with different immersing time.

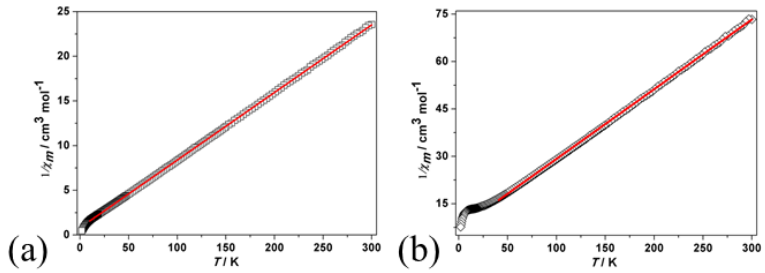

Figure S7. Plots of $1/x_m$ vs. T in the 2−300 K temperature range for **1** (a) and for **5** (b). The red solid line is the best fit to the Curie-Weiss law above 10 K for **1** and above 40 K for **5**.

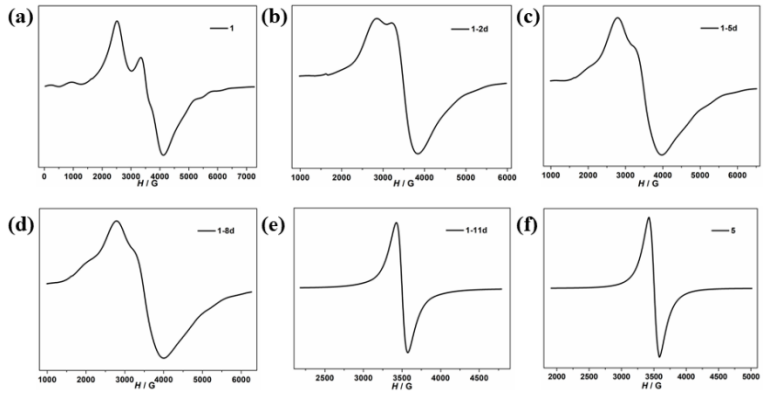

Figure S8. X-band EPR spectra of **1**, **1-2d**, **1-5d**, **1-8d**, **1-11d** and **5** measured at room temperature.

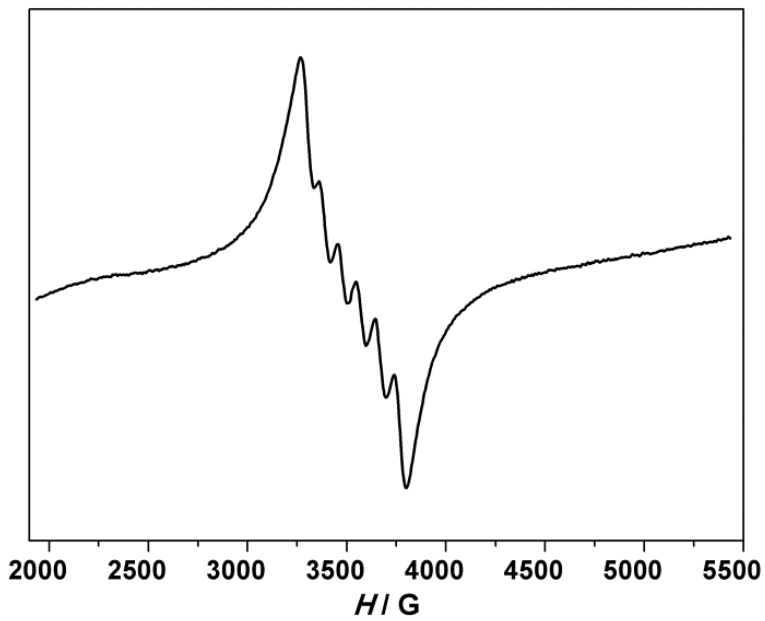

Figure S9. EPR spectra of methanol solvent after immersion sample **1** for 12 h.

4 Supplementary References

(1) Sheldrick, G. M., SHELXL-97, Program for X-ray Crystal Structure Refinement.; University of Göttingen, Germany. 1997.

(2) Sheldrick, G. M., Crystal structure refinement with SHELXL. *Acta Crystallogr. Sec. C: Struct. Chem.* **2015,** 71, 3-8.

(3) Spek, A. L., Structure validation in chemical crystallography. *Acta Crystallogr. Sec. C: Struct. Chem.* **2009,** 65, 148-155.

(4) Escuer, A.; Cordero, B.; Solans,X.; Font-Bardia, M.; Calvet, T., Manganese(II) Trimeric Systems Derived from Pyridyldioximato Ligands: Synthesis, Crystal Structure, and Magnetic Characterization. *Eur. J. Inorg. Chem.* **2008**, 5082-5087.

(5) Baca, S. G.; Malaestean, I. L.; Keene, T. D.; Adams, H.; Ward, M. D.; Hauser, J.; Neels, A.; Decurtins, S., One-Dimensional Manganese Coordination Polymers Composed of Polynuclear Cluster Blocks and Polypyridyl Linkers: Structures and Properties. *Inorg. Chem.* **2008**, *47*, 11108-11119.

(6) Menage, S.; Vitols, S. E.; Bergerat, P.; Codjovi, E.; Kahn, O.; Girerd, J. J.; Guillot, M.; Solans, X.; Calvet, T., Structure of the Linear Trinuclear Complex $Mn^{II}_3(CH_3CO_2)_6(BPY)_2$ Determination of The J Electron-Exchange Parameter Through Magnetic-Susceptibility and High-Field Magnetization Measurement. *Inorg. Chem.* **1991**, *30*, 2666-2671.

(7) Gomez, V.; Corbella, M., Versatility in the Coordination Modes of n-Chlorobenzoato Ligands: Synthesis, Structure and Magnetic Properties of Three Types of Polynuclear Mn^{II} Compounds. *Eur. J. Inorg. Chem.* **2009**, 4471-4482.

(8) Milios, C. J.; Stamatatos, T. C.; Kyritsis, P.; Terzis, A.; Raptopoulou, C. P.; Vicente, R.; Escuer, A.; Perlepes, S. P., Phenyl 2-Pyridyl Ketone and Its Oxime in Manganese Carboxylate Chemistry: Synthesis, Characterisation, X-Ray Studies and Magnetic Properties of Mononuclear, Trinuclear and Octanuclear Complexes. *Eur. J. Inorg. Chem.* **2004**, 2885-2901.

(9) Bu, X. H.; Tong, M. L.; Xie, Y. B.; Li, J. R.; Chang, H. C.; Kitagawa, S.; Ribas, J., Synthesis, Structures, and Magnetic Properties of the Copper(II), Cobalt(II), and Manganese(II) Complexes with 9-Acridinecarboxylate and 4-Quinolinecarboxylate Ligands. *Inorg. Chem.* **2005,** *44*, 9837-9846.